Light Emitting Diodes Based Photoacoustic and Ultrasound Tomography: Imaging Aspects and Applications

Kalloor Joseph Francis, Yoeri E. Boink, Maura Dantuma, Mithun Kuniyil Ajith Singh, Srirang Manohar, and Wiendelt Steenbergen

Abstract Tomographic photoacoustic and ultrasound imaging is essential for isotropic spatial resolution and to obtain a full view of the target tissue. However, tomographic systems with pulsed laser sources and custom made transducer arrays are expensive. Additionally, there are other factors that limit the wide use of photoacoustic and ultrasound tomographic systems which include the size of the tomographic systems that use pulsed laser and the laser safety issues. A cost-effective, compact and safe photoacoustic and ultrasound tomographic system can find several imaging applications both in clinics and small animal labs. LED-based photoacoustic imaging has shown the potential to bring down the cost, enable faster imaging with high pulse repetition rate and is safer when compared to pulsed lasers. The conventional US system can be adopted for photoacoustic imaging by adding a light source to it. Hence, linear transducer arrays are preferred as they are cheaper and allow faster

K. J. Francis (✉) · Y. E. Boink · M. Dantuma · W. Steenbergen
Biomedical Photonic Imaging Group, Technical Medical Center,
University of Twente, Enschede, The Netherlands
e-mail: f.kalloorjoseph@utwente.nl

Y. E. Boink
e-mail: y.e.boink@utwente.nl

M. Dantuma
e-mail: m.dantuma@utwente.nl

W. Steenbergen
e-mail: w.steenbergen@utwente.nl

K. J. Francis · M. Dantuma · S. Manohar
Multi-Modality Medical Imaging Group, Technical Medical Center,
University of Twente, Enschede, The Netherlands
e-mail: s.manohar@utwente.nl

Y. E. Boink
Department of Applied Mathematics, University of Twente, Enschede, The Netherlands

M. Kuniyil Ajith Singh
Research & Business Development Division, Cybedyne Inc.,
Cambridge Innovation Center, Rotterdam, The Netherlands
e-mail: mithun_ajith@cyberdyne.jp

M. Kuniyil Ajith Singh (ed.), *LED-Based Photoacoustic Imaging*,
Progress in Optical Science and Photonics 7,
https://doi.org/10.1007/978-981-15-3984-8_10

imaging. The combination of LED-based illumination and linear transducer array-based tomographic imaging can be a cost-effective alternative to current tomographic imaging, especially in point-of-care applications.

1 Introduction

In photoacoustic (PA) imaging, pulsed (nanosecond) light induces thermoelastic expantion in optical absorbers, resulting in acoustic signal generation. Detection of these optically excited acoustic signals for imaging enables optical absorption contrast at ultrasound (US) resolution [1, 2]. This imaging modality can surpass the high optical scattering with the detection of less scattered acoustic signals. Hence, it is a preferred modality where optical contrast, larger imaging depth, and high resolution are required [3]. PA tomography is one of the widely used configurations for deep tissue imaging where the target biological tissue allows a larger view angle [4, 5]. PA tomography has been demonstrated for applications such as breast cancer imaging [6, 7], thyroid cancer imaging [8], finger joint imaging [9], brain functional imaging [10], and small animal whole-body imaging [11]. An additional advantage of PA imaging is that it can be combined with US imaging as the same transducer can be used for both modalities [3, 12–14]. The visualization of PA images in the context of well known US images, with their complementary nature combining structural and functional information is of added value for clinical applications [3, 15]. Major limitations of tomographic systems are its cost, large size and safety issues with the use of pulsed laser sources [16]. Additionally, the large number of transducers and acquisition channels in tomographic systems also contribute to its size and cost. Hence, there is an urgency for cost-effective, compact and safe to use systems for an increasing number of clinical applications [16].

System cost and size of PA tomography systems can be considerably reduced by replacing pulsed Q-switched lasers with alternative sources such as laser diodes or LEDs [17]. Recent developments in LED-based PA imaging has shown promise in developing systems which are portable, safe to eye and having high frame rate [18]. A commercial system with LED-based illumination and linear US transducer is available for research applications [18]. This system is an example which shows that conventional US systems can be combined with PA imaging by simply plugging in a light source [18, 19]. An advantage of such a configuration is that with a software update, widely used US systems can incorporate PA imaging and can find faster clinical acceptance [19]. Another aspect is the use of linear transducer array instead of custom-developed transducers for tomographic imaging. The wide use of linear array and its production in large numbers resulted in high yield and low cost. Additionally, it enables faster US imaging with switching on and off subsets in an array for transmission [20]. While for PA imaging the whole array can simply be in the receive mode [20]. The usage of linear array also allows the use of less computational complex reconstruction methods such as the Fourier domain algorithm

[21]. Using the conventional US systems with linear array and low-cost illumination sources such as LEDs for tomographic imaging can enable cost-effective, compact and faster imaging systems.

2 Tomographic Imaging Using Linear Array

Linear transducer arrays are one of the first choices for tomographic imaging from its very beginning, starting with Oraevsky et al. in [22]. The factors which enabled the widespread clinical use were its availability in various frequency ranges, low cost, and ease of integration [23]. However, due to limited aperture and directional sensitivity of the linear transducer array, imaging suffers from loss of structural information, anisotropic resolution and artifacts [23]. In order to overcome the limited view problem, several methods were suggested. The use of a reverberant cavity by Cox et al. [24] and two planar acoustic reflectors at an angle by Li et al. [25] are some of the examples. However, the detected field of view in these proposed methods is limited and multiple artifacts degrade the image quality making it challenging in a practical setting. Scanning the transducer still remains a viable option for high-quality tomographic imaging at the expense of scanning time.

A combined PA and US imaging by circular scanning of the linear transducer was first studied by Kruger et al. in [26]. Two transducer scanning modes were used for tomographic PA and US imaging, as shown in Fig. 1 [27]. Rotating the long axis of the transducer about a center for imaging results in 2D imaging and rotating the shorter axis provides 3D imaging [27]. In the 2D imaging case, multiple views of the same imaging plane in a target tissue can be obtained by circular scanning of the transducer. In this case, the tomographic image can be formed either by a combined acoustic reconstruction from all the elements or by compounding B-scan images from individual views [23, 28]. In case of 3D imaging, the cylindrical focusing of the linear transducer array must be taken into account. This focus along the elevation direction

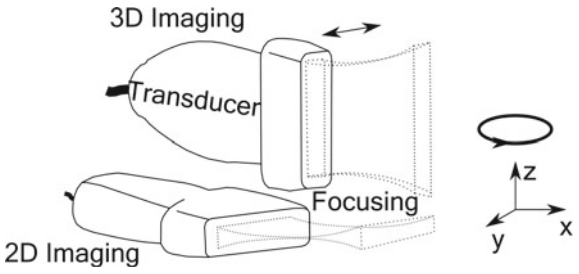

Fig. 1 Transducer configuration for 2D and 3D tomographic imaging. In the 2D imaging the long axis of the transducer is rotated around the sample. The imaging plane of the transducer with the cylindrical focusing is shown with doted lines. In the 3D imaging consists of linear scan at every angular location

results in imaging a different plane in each scan location. Combining these non-overlapping images from subsequent scan locations can result in discontinuities and smearing of structures [29]. To overcome these discontinuities in the 3D imaging, a translate-rotate scanning was proposed, where at each angular location a linear scan is performed [30, 31]. In this chapter, we are focusing on the 2D imaging configuration.

3 Imaging Aspects Using a Linear Array

The characteristics of the US transducer should be considered while designing the tomographic imaging configuration. Commercially available transducer arrays have acoustic focusing and directional sensitivity. The focus along the axial direction and the focus-zone where the transducer response is uniform should be considered to define the center of rotation and imaging area [26]. Further, the directivity of the transducer should be considered when defining the angular steps for the scanning. In this section, we present ultrasound transducer characterization results, followed by numerical simulations to determine an optimal number of angular views for tomographic imaging. We also present our image reconstruction approach and analysis of resolution improvement with tomographic imaging.

3.1 Transducer Characterization

AcousticX system (Cyberdyne Inc., Japan) was used in this work for both PA and US imaging. We have considered a linear transducer array with 128 elements having a center frequency of 7 MHz and a −6 dB bandwidth of 4–10 MHz, with a pitch of 0.315 mm. The transducer was first characterized to measure the directivity and focus. The characterization was performed in an acoustic receive mode. A 30 μm thick black suture wire (Vetsuture, France) was used as a PA target with LED-based illumination. We have used an LED array, illuminating at 850 nm wavelength with a pulse energy of 200 μJ and a pulse duration of 70 ns. The PA source was fixed and using motorized stages the transducer was moved to various axial and lateral locations. In the first experiment, the focus of the transducer was measured. The PA source was aligned to the short axis of one of the center elements of the transducer. The raw PA signal from the line target was acquired and the peak-to-peak value was plotted against the distance between the transducer and the PA source. The measurements were repeated for varying the axial distance between the transducer and the PA source. Figure 2a shows the peak-to-peak value of the PA signal at different axial positions. From the plot, the maximum PA signal value (3.5×10^4) was observed at 20 mm which is the focus of the transducer. On either side of the focus, a uniform drop of PA signal intensity to a value of 2.8×10^4 was observed. A similar pattern was observed by Kruger et al. [26]. They considered the focus of the transducer as the center of rotation for tomographic imaging and the uniform region for imaging. The same approach

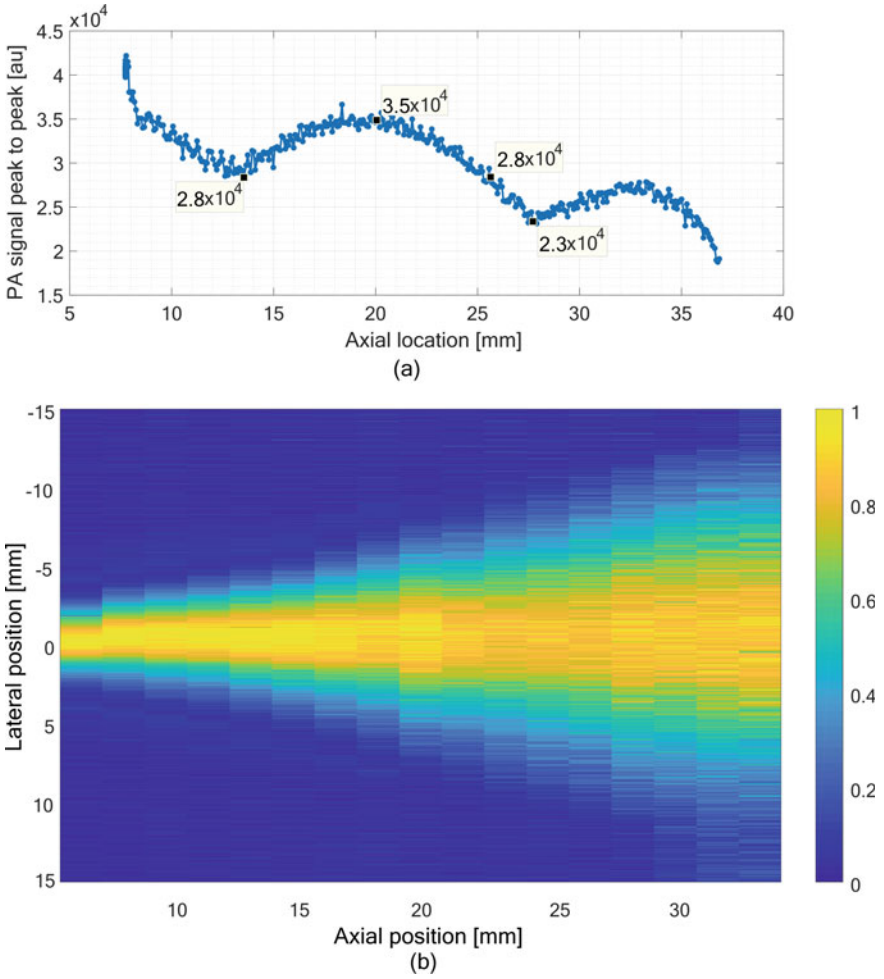

Fig. 2 Transducer characterization. **a** Axial response of the transducer. **b** Acoustic field of a single element

was adopted in our study. We have considered the focus distance (20 mm) to define the center of rotation with a ±5 mm window within the uniform region (15–25 mm) in the axial response of the transducer for larger and smaller samples.

In the second experiment, the directional sensitivity of a single element in a transducer array was measured. The transducer was scanned in both lateral and axial direction and peak PA signal values were recorded for one of the center elements. Figure 2b shows the PA intensity at different lateral and axial locations. At each depth with a Gaussian fit on the measured data, the Full Width Half Maximum (FWHM) was calculated. The angle made by the FWHM point with the center of the transducer element was calculated to be $26.8 \pm 0.2°$. To obtain the combined

directivity of the transducer, the acoustic field of individual elements were combined together. The opening angle on either side of the transducer was calculated in a similar fashion using the FWHM points. The combined directivity of the transducer was estimated to be $16.6° \pm 1.5°$. The opening angle of a single element need to be considered for PA mode as well as conventional line-by-line B-mode US imaging as all elements are in the receiving mode. In the plane wave US mode, the directivity of the whole transducer needs to be considered, as US transmission from all the elements is involved in this mode.

3.2 Optimal Number of Angular Views

A target structure placed at an angle with the transducer is detectable if the normal from it falls within the opening angle of a transducer element [32]. Hence, with the opening angle of $26.8° \pm 0.25°$ to detect a structure with an arbitrary angle, a minimum of 14 views are required to cover the entire 360°. While in the case of plane wave US imaging, with the opening angle of the transducer being $16.6° \pm 1.57°$, 24 angular views are required to have full-view tomographic imaging. This theoretical estimation is a minimum as the transducer directivity is not a sharp cutoff function. Hence, we performed an acoustic simulation to study the number of angular views required to obtain an adequate image quality in the tomographic setting. A phantom was designed for the simulation study as shown in Fig. 3a. Considering the tomographic imaging we would like to test whether structures having different orientations can be reconstructed well. Angular dependency was incorporated in the phantom with 24 line targets placed at 15° angular steps as shown in Fig. 3a. Next, we considered targets with different sizes to test the resolution enhancement with tomographic imaging. Line targets and circular disks of different sizes were considered in the phantom to make it resolution dependent. Given a center-frequency (f_0) of the transducer and the corresponding wavelength (λ_0), a typical resolution of $\lambda_0/2$ is expected from the transducer. In our experiments with the center frequency of 7 MHz and a bandwidth of 4–10 MHz, the second set of structures were incorporated in the phantom with different thickness varying from $\lambda_0/4$, $\lambda_0/2$, λ_0, $2\lambda_0$ to $4\lambda_0$. The circular targets of diameter $\lambda_0/2$, λ_0, $3\lambda_0/2$ and $2\lambda_0$ were also placed in the phantom. Further, four different levels of initial pressures were also included making it ideal phantom for image quality based study.

Acoustic wave propagation was performed using k-Wave toolbox of MATLAB [34]. A homogeneous acoustic medium mimicking water with a speed of sound of 1502 m/s and a density of 1000 kg/m^3 was used in the forward model. The transducer elements were modeled to have finite size with spatial averaging of point detectors with a directivity mask [34]. Gaussian noise with a signal to noise ratio of 50 dB, with the signal level taken as the Root Mean Square (RMS) value of the raw acoustic signal was generated and added as the measurement noise. The simulation was repeated for different number of angular views with the linear array around the phantom. Individual B-scan images were formed from each angular view using the Fourier

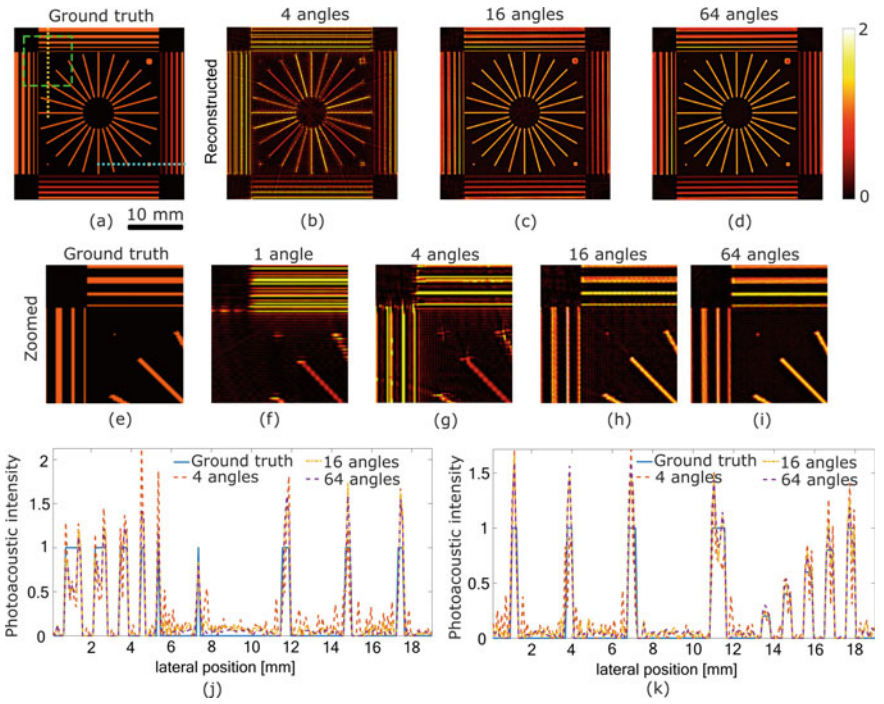

Fig. 3 Image quality versus angular views. **a** Ground truth photoacoustic phantom. **b**, **c** Reconstructed images from 4, 16 and 64 angular views. **e** Zoomed in region of the phantom, marked with the green box in (**f**–**i**) and the corresponding reconstructed images from 1, 4, 16 to 64 angles respectively. **j**, **k** Line profiles from a vertical (yellow) and a horizontal (blue) region, comparing ground truth and reconstructed photoacoustic pressure (Reproduced with permission [33])

domain reconstruction algorithm [35]. The tomographic image was formed by spatial compounding of B-scan images from all angles. We have chosen structural similarity (SSIM) index [36] and peak signal-to-noise ratio (PSNR) to measure the image quality of the reconstructed image with respect to the ground truth. We have selected SSIM to check how well the structures are reconstructed and PSNR to measure the signal to the noise level in the image. Figure 3b–d shows reconstructed images from 4, 16 and 64 angular views respectively. A zoomed-in region (marked in green) of the ground truth and reconstructed images from 1, 4, 16 to 64 angles are provided in Fig. 3e–i. In imaging using a single view only horizontal line targets are reconstructed. This limited view problem can also be observed in the circular targets, as only the top and bottom boundaries were reconstructed. Calculated SSIM was 0.09 indicating low structural similarity. Additionally, the reconstructed image contains artifacts and measurement noise providing a poor PSNR value of 7. An additional view from 18° can only provide a small improvement in the image quality as no additional angular information is available. With 4 angular views, SSIM improved to 0.3 and PSNR to 11, as all the vertical and horizontal structures are reconstructed. It can be observed

that structures with different intensity levels are also distinguishable. However, the circular targets are not fully reconstructed and the noise level is still high. From 4 to 16 views there is a linear increase in reconstructed image quality. In case of tomographic image with 16 number of angular views all the structures at different angles, intensity levels and sizes are resolved well with providing an SSIM of 0.53 and the noise and artifacts are much lower with a PSNR value of 15.3. Further increasing the number of views has little impact on the image quality with SSIM change from 0.52 to 0.56 for the number of angular views from 16 to 64. The line profiles in Fig. 3j, k compares the ground truth to the reconstructed photoacoustic intensity. The profile in Fig. 3j shows line target with 5 different thickness, the smallest circular target and three line targets placed at different orientations. The reconstructed PA pressure levels are compared with that of ground truth. The profile in Fig. 3k shows targets with 5 different initial pressure levels and the corresponding reconstructed PA pressure levels. These line profiles also shows that from 16 number of views the structures can be reconstructed to a large extent and more views add less information. From this study based on image quality, we can conclude that 16 angular views in a step of 22.5° is optimal for tomographic PA image reconstruction. This is a good agreement with the theoretical estimate of 14 views made earlier. A small oversampling with angular steps of 20° resulting in 18 number of angular views were considered for the experimental study.

3.3 Tomographic Image Reconstruction

Tomographic image formation can be performed by combined acoustic reconstruction [23] or by spatial compounding of the B-scan images [28, 37]. We have considered multi-angle spatial compounding to form tomographic photoacoustic and ultrasound images [28]. The PA and US signals were acquired using the linear transducer array by scanning around the sample as shown in Fig. 5a, b. The PA and US data from each angle are first reconstructed to form B-scan images. The B-scan images formed directly from the system using an in-built real-time reconstruction algorithm. This can also be performed off-line using a similar Fourier domain algorithm [35, 38]. Additionally, the system can perform both plane wave and B-mode US imaging. The B-scan images were then rotated to the corresponding angle they were acquired. An image rotation was performed to correct for the angle it was acquired. The rotated images are then averaged to obtain the tomographic image.

3.4 Resolution Improvement

Imaging using a linear array with a single view of the target results in an asymmetric resolution along the axial and lateral direction. A higher resolution can be achieved along the axial direction compared to the lateral, as the resolution along axial direction depends only on the bandwidth of the transducer [39]. There are two factors that

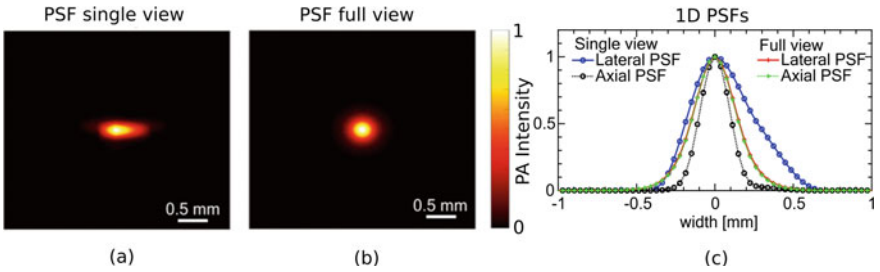

Fig. 4 Photoacoustic Point Spread Function (PSF) obtained from 30 μm target. **a** Normalized PSF from a single view with the linear array. **b** Normalized PSF from tomographic imaging obtained from 18 angular views. **c** Comparison of 1D PSF extracted from (**a**) and (**b**) along the lateral and axial direction

degrade the lateral resolution. First, the finite size of the element results in a spatial averaging of the received acoustic signals [39]. Second, the reconstruction from limited view measurements causing artifacts along the direction where detectors are absent [40]. Reconstruction from a full-view tomographic measurement can improve the resolution with projections from all the angles. Resolution improvement in tomographic imaging using a linear array was reported by Kruger et al. [41] with simple compounding of B-scan images from different angles. A small improvement in resolution was claimed with combined image reconstruction from all the measurements [42] and with the use of multi-view Hilbert transform [23].

We have performed Point Spread Function (PSF) measurements in PA mode with a single view and with tomographic imaging from 18 views. A suture wire (Vetsuture, France) with a diameter of 30 μm was used as PA target and an 850 nm LED array as illumination source. Figure 4a shows PSF from a single view. Measured axial Full-Width Half Max (FWHM) was 0.22 mm and lateral FWHM was 0.47 mm. PSF from tomographic reconstruction using spatial compounding of 18 angular views is shown in Fig. 4b. The PSF is symmetric and the axial and lateral resolution were measured to be 0.31 mm. A detailed analysis of 1D PSF along the lateral and axial direction for both single view and the tomographic case is shown in Fig. 4c. It can be observed that spatial compounding provides an improvement in lateral resolution at the expense of degrading the axial resolution. However, it is possible to obtain an isotropic resolution and limited view artifacts can be removed.

4 LED-Based Illumination for Tomography

In this section we present the illumination configurations using LED arrays. We also performed simulations to study the light propagation from the LEDs into soft tissue and present tomographic imaging results using the illumination configuration. The AcousticX system used in this study can drive four LED units simultaneously. While

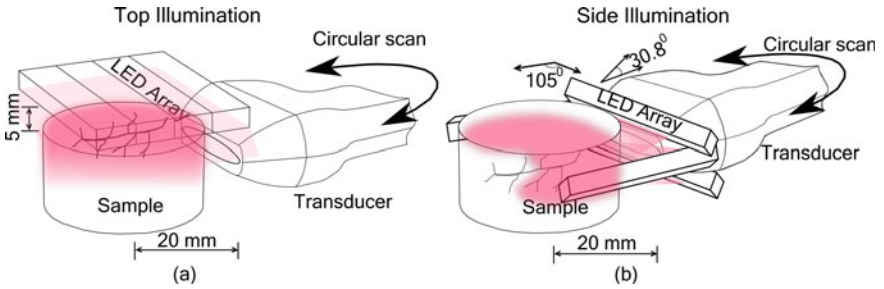

Fig. 5 Tomographic imaging configurations with **a** illumination from the top of the sample and **b** illumination from the sides of the sample (Reproduced with permission [33])

in the normal hand-held configuration only two LED units are used. Tomographic imaging demands more energy for better penetration depth. Hence a combination of all four LED units were considered for illumination. Each LED unit consists of 144 elements arranged in an array of 36 × 4 with an active area of 55 × 7 mm with an energy of 200 μJ per pulse. Two LED configurations are presented in this work. The first one is for applications where the top of the sample can be accessed for illumination, such as brain functional imaging [43]. The second configuration is for samples that can only be accessed from its sides, such as finger joint imaging or small-animal whole-body imaging. A schematic of the illumination configurations is provided in Fig. 5.

To study the fluence distribution in a soft tissue using these two illumination configurations, combined optics and acoustic simulations were performed. The light propagation from LED array into the tissue was modeled using Monte Carlo simulation with Monte Carlo eXtreme (MCX) photon transport simulator [44]. A cylindrical phantom with a 25 mm diameter in water having average soft tissue optical tissue properties ($\mu_a = 0.56\,\text{mm}^{-1}$, $\mu_s = 9.9\,\text{mm}^{-1}$, g = 0.90, n = 1.4) [45] was considered in these simulations. The LED elements were modeled with a solid opening angle of 120°. In the top illumination case, four adjacent LED units were positioned at a distance of 5 mm above the phantom as depicted in Fig. 5a. While for illumination from the side, two LED bars were placed above and below the transducer's active part, with an angle of 30.8° such that the illumination intersect the focus of the transducer (at 20 mm) in a non-scattering medium. Additionally, two more LED bars with an angle of 105° relative to the transducer array were placed in the imaging plane. To reflect the acoustic signals away from the transducer and to minimize artifact, the LED arrays were placed in an angle of 5° with the imaging plane.

The fluence maps from the Monte Carlo simulations were then coupled with the acoustic simulation. To obtain the initial pressure, the ground truth was multiplied with normalized fluence map. A plane 5 mm inside cylindrical phantom was considered for the fluence map. The Grüneisen parameter was not considered here, as we were interested only in the spatial variation of initial pressure and not in its absolute value. For the ground truth a vascular structure from a retinal image in the

DRIVE database was used [46]. To mimic soft tissue acoustic properties, a speed-of-sound of 1580 m/s and density of 1000 kg/m^3 were used for the phantom. For the coupling medium we assigned a speed-of-sound of 1502 m/s and a density of 1000 kg/m^3. The acoustic attenuation was modeled as power-law with pre-factor chosen to be 0.75 dB/(MHz$^{1.5}$ cm). The directivity and bandlimited nature of the transducer was also modeled as explained in the previous simulation (Sect. 3.2). The first-order k-space model was used for forward acoustic wave propagation. To mimic measurement noise, Gaussian noise with SNR of 30 dB (with respect to the RMS value of the PA signal) was added to the RF signals. For a realistic scenario the spatial variations in the acoustic properties are unknown. Hence, for the reconstruction, we assumed an uniform acoustic properties. The tomographic images were formed by spatial compounding of reconstructed B-scan images from all the angles. A normalization was performed on the reconstructed images such that the total intensity of the vascular structures are the same as that of the ground truth [47]. The normalization was performed by segmenting the pixels in the region of the vascular structures and normalizing such that the sum of pixel values in the segmented region is equal to that of the ground truth. Tomographic images obtained from top and side illuminations were compared validated against the ground truth.

A uniform illumination is desired to view the whole sample from all the angles and to form a perfect tomographic image. In this simulation study, we compare the difference in reconstructed image from a fixed top illumination and rotating side illumination. Figure 6a and b show optical fluence map from the top and side illumination. A line profile of the fluence map extracted from the center of the phantom is also shown below images. In the top illumination, the fluence is mostly uniform. An asymmetric drop of the fluence at the edges of the phantom in the vertical direction can be observed compared to the horizontal. This asymmetry is due to the rectangular (50 mm $\times$ 40 mm) illuminated region, as we stacked LED units. From the center of the phantom to the edge a maximum drop in fluence of 46% was observed. In the case of side illumination, the fluence dropped to 30% at the center compared to the one at the boundary.

The ground truth vascular phantom is shown in Fig. 6c. The initial pressure map from top and side illumination, obtained by multiplying the ground truth with the fluence map (Fig. 6a, b) is shown in Fig. 6d, e. Tomographic images obtained from 16 angular views are shown in Fig. 6f, g. In both the configurations, all the structures in the phantom were reconstructed. Figure 6f shows that with top illumination, the reconstructed pressure level is lower towards the boundary of the phantom compared to the center. While for side illumination in Fig. 6g, the reconstructed pressure is lower at the center of the phantom, compared to the rim. This is further evident in the line profiles in Fig. 6h, i, extracted from the reconstructed images along the vertical (white) and horizontal (green) lines through the center of the phantom. The speed-of-sound is considered uniform in the reconstruction. As a result of this assumption, a lateral shift in the peaks compared to the ground truth can be observed in the line profiles. In the tomographic imaging utilizing spatial compounding of B-scan images, this can result in smear artifacts from multiple angles and a change in the size of the structures. To concluded, both configurations can be used for tomographic

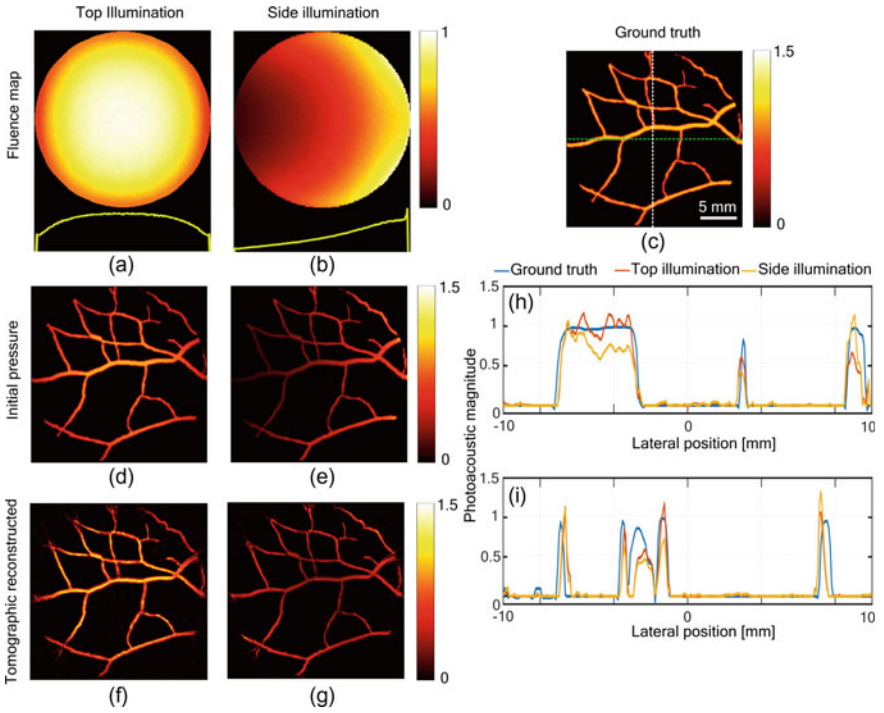

Fig. 6 A simulation study comparing top and side illumination configurations. **a**, **b** Normalized optical fluence maps in the two cases respectively. A line profile of the fluence map extracted from the center of the phantom is shown below the image. **c** Ground truth vascular phantom. **d**, **e** Initial pressure obtained from top and side illumination respectively. **f**, **g** Reconstructed and normalized tomographic images from 16 angular views. **h**, **i** Comparison of line profiles between the ground truth (**c**) and the reconstructed images (**f**) and (**g**), along horizontal (green) and vertical (white) lines passing through the center of the phantom respectively (Reproduced with permission [33])

imaging. However, with top illumination, a region of interest around the center can be reconstructed well. This aspect can be helpful in applications like small animal brain imaging. In the case of side illumination, there is a significant amount of overlap in the illuminated regions between angular views. This overlapping illumination region allows multiple view of the same structure enabling tomographic reconstruction. The lower fluence at the center of the sample can result in a lower reconstructed pressure level in this region. However, with more number of transducer elements observing the center higher SNR can be obtained with averaging. Using the side illumination the rim of the object is illuminated fairly uniform. Hence side illumination can be potentially used for finger joint tomographic imaging.

4.1 Imaging Experiments

The illumination configurations developed in Sect. 4, and scanning steps for tomographic imaging using a linear array determined in Sect. 2, were incorporated in the experimental setup. In this section, we present imaging using the two LED array configurations. We also discuss the imaging speed our tomographic system.

4.2 Tomographic Imaging Using Top Illumination

In the first configuration, all the four LED units are stacked together to form a large array of 576 elements, placed 5 mm above the sample for uniform illumination. In this case, the illumination is static and only the transducer is rotated around the sample for tomographic imaging. Uniform illumination of the entire sample for all angular views is ideal for tomographic imaging as this enables the transducer to view the same structure from different angles. To a large extent, this is possible with the illumination from the top of the sample.

Figure 7a shows a photograph of a leaf skeleton stained with India ink and included in a 3% agar phantom. The leaf phantom was selected as it has structures of different thickness and orientation for a resolution study in the tomographic setting. Additionally, the structures in the leaf mimic typical vascularization such as the one in small animal brain [43]. PA imaging of these structures indicates the applicability of this imaging system. Figure 7b–g shows B-scan PA and US images from three angular views. These images show the structure of the leaf with the limited view from a linear array. Structures which are having smaller angles with the transducer are reconstructed well. This shows the need for tomographic imaging to obtain a full view of the sample. Figure 7h, i show the PA and US tomographic images respectively. A zoomed-in image of the leaf in Fig. 7j shows four levels of structures based on the thickness. It can be observed in Fig. 7k–m, that with increasing number of angular views from 4, 12 to 18, finer structures are visible. Three levels of structures are reconstructed with 18 angular views leaving only the smallest structures in the leaf undetected. The smallest structures were not reconstructed as the bandwidth of the transducer is limited and the high frequency components in the PA signals were not detected. The tomographic US image formed with the plane-wave mode in Fig. 7c shows the boundary of the leaf and the larger veins. It should be noted that the number of angular views of 18 is insufficient in the plane wave mode for a complete tomographic imaging and the specular nature of the imaging is not appropriate to differentiate these structures.

It is also possible to image ex vivo tissue samples of small size using this configuration. A typical example is surgically excised tissue to look for malignancy before pathological inspection [39]. In another experiment, we have imaged an ex vivo mouse knee sample. In this case, we also compared the difference in tomographic US imaging using the plane wave and conventional line-by-line scanned B-mode.

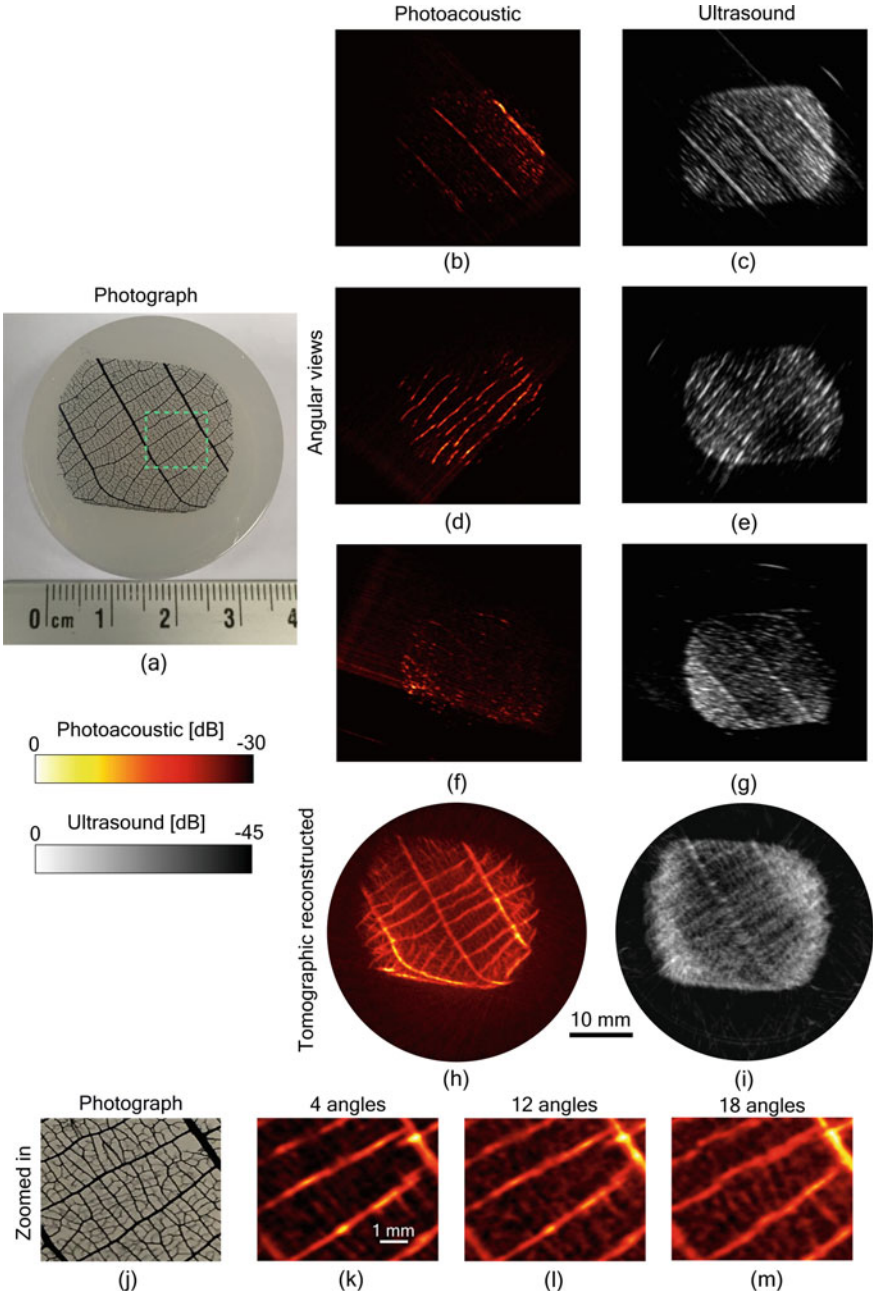

Fig. 7 Tomographic imaging of a leaf skeleton. **a** Photograph of the leaf. **b**, **d**, **f** Photoacoustic B-scan image from three angles. **c**, **e**, **g** Ultrasound B-scan image from three angles. **h** Photoacoustic tomographic image from 18 angular views. **i** Ultrasound tomographic image from 18 angular views. **j** Zoomed in region of the leaf skeleton indicated by green box and (**k**)–(**m**) are PA tomographic image of the zoomed in region using 4, 12 and 18 angular views (Reproduced with permission [33])

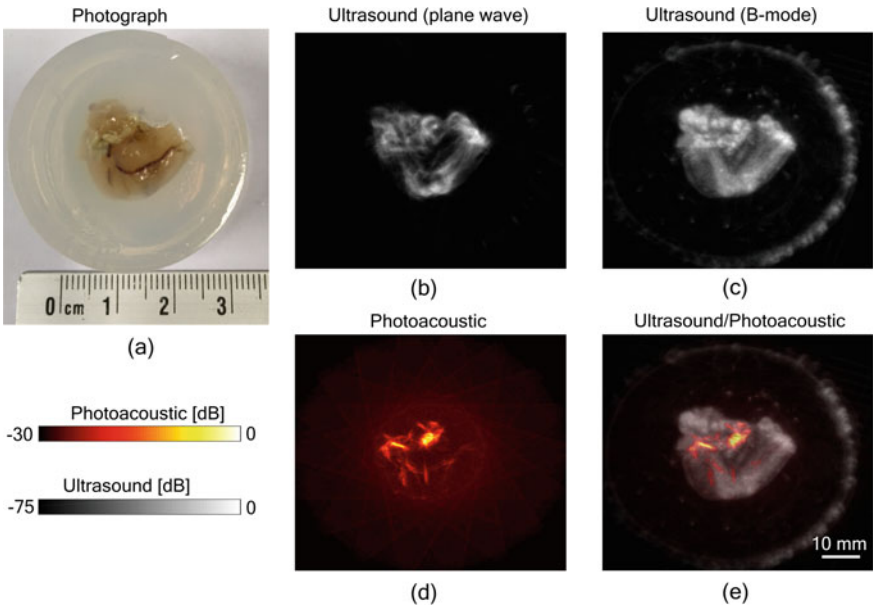

Fig. 8 Mouse knee imaging. **a** Photograph of the ex vivo mouse knee sample. US tomographic images obtained from **b** plane wave imaging and **c** B-mode imaging. **d** PA image of the sample. **e** Combined PA and US image (Reproduced with permission [33])

Figure 8a shows the mouse knee sample embedded in a 3% agar phantom. Figure 8b shows tomographic US imaging using the plane wave mode and Fig. 8c using B-mode. Tomographic imaging using B-mode US shows superior quality in its compared with the case of plane wave. Two bones forming the joint and the tissue around it are visible in the tomographic image. Adding more angular views can improve the plane wave ultrasound-based tomographic image. A major blood vessel running through the joint is visible in the photograph in Fig. 8a. The PA image in Fig. 8d shows the blood vessel and several branches from it. There are some discontinuities as the blood vessel was not completely in the imaging plane. Additionally, clotted blood near the point where the joint was dissected is also visible as a high absorbing spot. The coregistered PA and US tomographic image in Fig. 8e shows both joint and blood vessels. The capability to visualize both vascular development and joint damage can be useful for early detection of rheumatoid arthritis.

4.3 Finger Joint Imaging Using Side-Illumination

Rheumatoid Arthritis (RA) is an autoimmune disorder affecting joints, which leads to disabilities [48]. If not detected and treated at an early stage, the disease can per-

manently damage the joints. Imaging the synovium to identify inflammation and angiogenesis can indicate the disease activity. US and magnetic resonance imaging (MRI) are used for imaging joints. US imaging is less sensitive to early stage changes in the synovium. The vascularization of the synovium is imaged using Ultrasound power Doppler (US-PD) [49]. However, lack of sensitivity to small blood vessels limits the applicability of US-PD. MRI can provide good visuaization of the synovium. However, it is largely inaccessable, expensive and needs contrast agents [49]. In this scenario, PA imaging has shown the potential to detect vascularization in the synovium with the high optical absorption of the blood [49]. Physiological biomarkers in the synovial tissues such as neoangiogenesis, hypoxia and hyperemia can be detected using PA imaging [50]. Therefore, PA imaging can be used for joint imaging for RA and other rheumatologic conditions such as osteoarthritis, crystal deposition diseases, seronegative spondyloarthropathies, and systemic lupus [48]. There are many efforts to use low-cost and compact light sources in PA imaging systems, specifically for the application of RA [48, 49]. The primary goal is to have a compact PA system as a point-of-care device in the vicinity of a rheumatologist. Patient studies using LED [51] and laser diode [49] based PA illumination added to conventional US systems have shown promise in point-of-care imaging for RA monitoring. However, these handheld systems using linear transducer arrays can miss early signatures of RA due to the asymmetric resolution and limited view. Hence, a tomographic system is needed to obtain a full view of the target tissue [52, 53].

We have developed a finger joint imager using the side illumination configuration explained in Sec. 4. A holder for the transducer and LED units with the configuration design developed in Sect. 4 was 3D printed. A schematic of the finger joint imager is shown in Fig. 9a. A translational stage with an accuracy of 100 μm with a maximum range of 157.7 mm and a rotational stage with a 0.1° accuracy for 360° rotation was used for scanning the imaging probe. Additionally, hand rest and a fingertip positioner were used to minimize movement during the scan. A photograph of the finger joint imager is shown in Fig. 9b. In a proof-of-concept experiment, a finger joint of a healthy female volunteer was imaged. Figure 9c shows combined PA and US images of a finger showing the interphalangeal joint and the blood vessels around it. Tomographic PA and US images were acquired at locations $p1$ at the joint, and $p2$ which is 5 mm away from the finger joint. Figure 9d–f are tomographic PA, US and combined images at $p1$. Figure 9g–i are tomographic PA, US and combined images at $p2$. The ultrasound images show a hypoechogenic region for both bone and blood vessels. The skin and the blood vessels are visible in the PA images. The interphalangeal joint in the US image ($p1$) shows two distinct regions in the bone with a narrow separation possibly from the curved region of the joint. Figure 9j shows tomographic PA images with increasing number of angular views from a partial view of 90° to a full-view acquired from 360°. This images shows the need for a full-view tomographic imaging. In this proof-of-concept study to minimize the imaging time for in vivo measurement plane-wave, US image was used. The use of B-mode and more angular views can improve image quality. The initial result shows that the

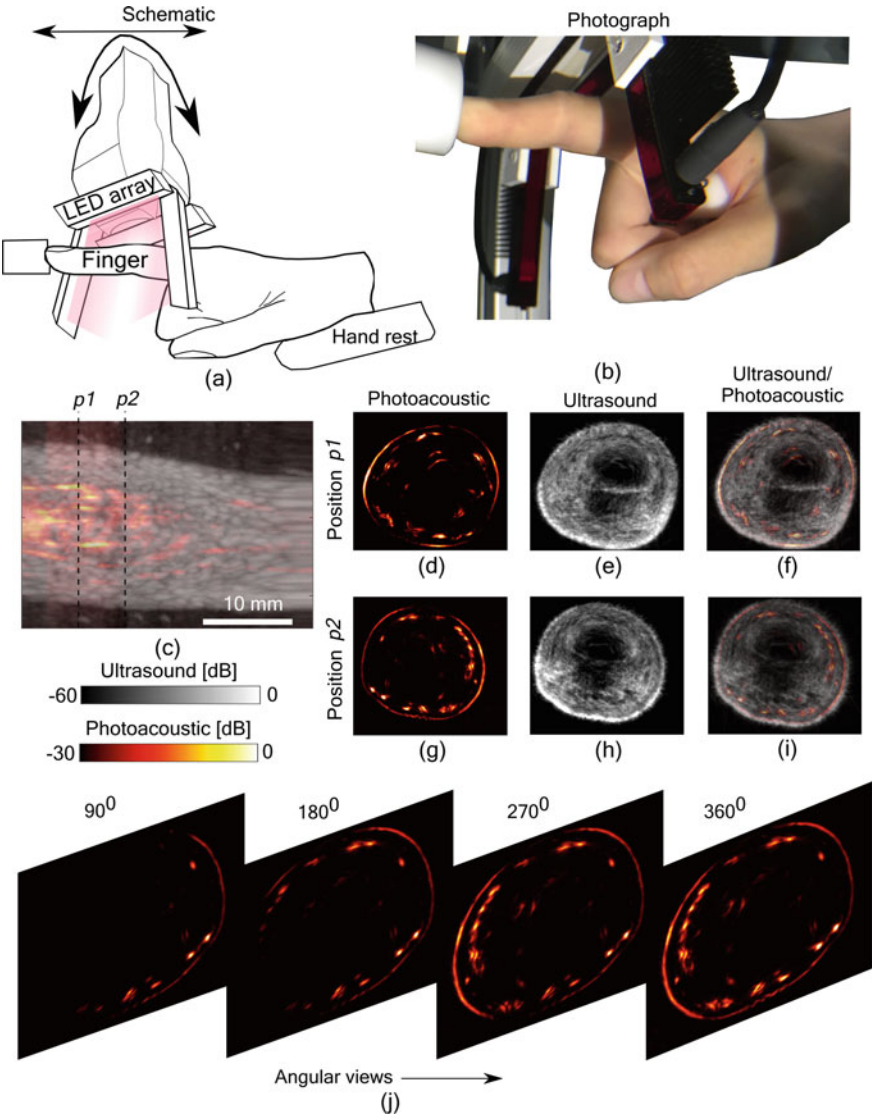

Fig. 9 Finger joint imaging. **a** Schematic and **b** photograph of the imager. **c** Combined PA and US image from a linear scan of the finger joint. **d**–**f** Photoacoustic, ultrasound and co-registered image respectively at position $p1$. **g**–**i** Photoacoustic, ultrasound and co-registered image respectively at position $p2$. **j** Tomographic photoacoustic images obtained from increasing number of angular views (Reproduced with permission [33])

tomographic US and LED-based PA system can be used to image the vascularisation around the finger joint and the bone structure, which shows its potential. To test the system for its applicability in RA imaging, an extensive patient study is required.

4.4 Tomographic Imaging Speed

In the AcousticX system, RF data from all US elements are acquired at a sampling rate of 40 MHz for US and at 20 MHz for PA imaging and transferred to the GPU board. Acquired data (US and PA) is reconstructed using an in-built Fourier-domain based reconstruction algorithm and then displayed in real-time. The system can drive the LED arrays as well as transmit and acquire data parallelly from all 128 elements of the US probe to generate interleaved PA and plane wave US images at a maximum frame rate of 30.3 Hz, with the maximum LED pulse repetition frequency (PRF) of 4 KHz which delivers the possibility of averaging more PA frames to attain good SNR without degrading the frame rate.

In our experiments at an LED PRF of 4 KHz, 64 PA frames are averaged on-board within the DAQ and then the data is transferred to AcousticX PC through the USB interface. This data is averaged 6 times in the PC and then reconstructed using a frequency-domain algorithm implemented in the GPU. One US (planewave) frame is acquired between every 64 PA frames to generate US and PA overlaid images at an interleaved frame rate of 10.3 Hz. After acquiring one PA and US image at the first angular view (97 ms), the imaging probe was rotated by 22.5° in 2.56 s and the next view was acquired. This was continued for 16 different angular views to attain 360° view, which is then used for generating a PA/US tomographic image. Thus, the total time required for generating a full view tomographic US/PA image is 42.5 s.

The system is also capable of performing conventional US line-by-line acquisition (transmit with 10 channels, receive with 16 channels) by scanning each line of an image for generating high quality B-mode US images along with PA images at the expense of frame rate (6.25 Hz compared to 10.3 Hz in the plane wave US). In the small animal cadaver experiment, this setting was used since high-speed scanning is not a prerequisite in this case. The total time required for generating a full view tomographic US/PA image is 43.5 s, which is almost a second slower than the acquisition involving plane-wave US imaging.

5 Future Perspectives

Our simulation, phantom, ex vivo and in vivo results give a direct confirmation that LED-based tomographic PA imaging using linear array US probes holds strong potential in multiple clinical and preclinical applications. However, several improvements are required for translating this technology to preclinical labs and clinics. The use of multispectral tissue illumination for obtaining blood oxygen saturation images is one of the key applications of PA imaging. By utilizing LED arrays of different wavelengths, we would like to explore this in our future studies in a tomographic setting. It is foreseen that 3D images of vasculature and oxygen saturation combined with anatomical information offered by US imaging would be a valuable tool for RA detection and staging in both preclinical and point-of-care clinical settings. Currently,

LED arrays are designed in such a way to fit well on both sides of a linear array US probe with an aperture close to 4 cm. In this work for tomographic imaging, we used a pseudo-arc-shaped illumination with commercially available LED matrices. However, a custom developed arc or ring-shaped LED array would be more appropriate for tomographic imaging applications. We would like to explore custom-developed LED arrays for specific applications such as small animal imaging in the future.

Another improvement we would like to incorporate into the system is on the US transducer. We have used a 7 MHz linear array probe in this work. For imaging deeper structures, we would like to use a transducer with low center frequency (1–3 MHz) with a wide bandwidth. From the PA images, we observed that blood vessels were visualized as double-layered features (only lumen) with no information inside the vessels. This is mainly because of the bandwidth limitation of the US probe. For accurate PA imaging, it is of paramount importance to design high bandwidth US probes in the future. This may help to visualize entire blood vessels, instead of walls as in conventional linear array US probe-based 2D PA imaging. Quantitative PA imaging will also be more accurate with an improved US transducer with high bandwidth.

From the application perspective, an update to the commercial system with circular scanning and tomographic image rendering would be useful for many labs to use the proposed tomographic imaging. This will enable the use of an LED-based system (AcousticX) in animal imaging facilities and pre-clinical labs for tomographic imaging. With all the above improvements in light delivery, acoustic detection, and circular scanning, we foresee to target small animal imaging (brain and abdomen) and several clinical applications (RA monitoring, breast imaging) in the future. An affordable, point-of-care full view tomographic imaging system with structural, functional, and molecular contrast is expected to have a significant impact in pre-clinical/clinical diagnostic imaging and treatment monitoring.

6 Conclusion

In this chapter, we have demonstrated that using LED-based illumination and a linear transducer array, tomographic photoacoustic and ultrasound imaging system can be performed. A method to determine the optimal number of angular views for a full view tomographic imaging is presented and it was validated with experimental results. In terms of penetration depth, the pulse energy from an LED is a limitation for tomographic imaging. Hence, we have demonstrated the use of 576 LED elements in two configurations in the tomographic setting. Both the configurations developed here have great potential biomedical imaging applications. We have successfully demonstrated the applicability of our method in joint imaging both in ex vivo samples and in vivo human finger. However, we restricted ourselves to imaging applications involving smaller samples ($\leq$30 mm), as the pulse energy is still a bottleneck for larger tissues. A tomographic imaging time using our system is mainly limited by the scanning time. Although the imaging takes less than a minute, this speed can

still be a limitation in some applications. Imaging speed is a trade-off factor that we considered to reduce the system cost. Provided that the longer pulse duration (10s of nanoseconds) is acceptable for photoacoustic imaging, this inexpensive, compact and safe to use tomographic system demonstrated in this work can find applications especially in point-of-care imaging.

References

1. S. Manohar, D. Razansky, Photoacoustics: a historical review. Advances in optics and photonics **8**(4), 586–617 (2016)
2. M. Xu, L.V. Wang, Photoacoustic imaging in biomedicine. Rev. Sci. Instrum. **77**(4), 041101 (2006)
3. K.J. Francis, S. Manohar, Photoacoustic imaging in percutaneous radiofrequency ablation: device guidance and ablation visualization. Phys. Med. Biol. **64**(18), 184001 (2019)
4. P.K. Upputuri, M. Pramanik, Recent advances toward preclinical and clinical translation of photoacoustic tomography: a review. J. Biomed. Opt. **22**(4), 041006 (2016)
5. L.V. Wang, Prospects of photoacoustic tomography. Med. Phys. **35**(12), 5758–5767 (2008)
6. S. Mallidi, G.P. Luke, S. Emelianov, Photoacoustic imaging in cancer detection, diagnosis, and treatment guidance. Trends Biotechnol. **29**(5), 213–221 (2011)
7. S. Manohar, M. Dantuma, Current and future trends in photoacoustic breast imaging. Photoacoustics (2019)
8. A. Dima, V. Ntziachristos, In-vivo handheld optoacoustic tomography of the human thyroid. Photoacoustics **4**(2), 65–69 (2016)
9. J. Jo, G. Xu, M. Cao, A. Marquardt, S. Francis, G. Gandikota, X. Wang, A functional study of human inflammatory arthritis using photoacoustic imaging. Sci. Rep. **7**(1), 15026 (2017)
10. D. Wang, Y. Wu, J. Xia, Review on photoacoustic imaging of the brain using nanoprobes. Neurophotonics **3**(1), 010901 (2016)
11. J. Xia, L.V. Wang, Small-animal whole-body photoacoustic tomography: a review. IEEE Trans. Biomed. Eng. **61**(5), 1380–1389 (2013)
12. K.J. Francis, E. Rascevska, S. Manohar, Photoacoustic imaging assisted radiofrequency ablation: illumination strategies and prospects, in *TENCON 2019 IEEE Region 10 Conference* (IEEE, New York, 2019)
13. N. Rao, K.J. Francis, B. Chinni, Z. Han, V. Dogra, Innovative approach for including dual mode ultrasound and volumetric imaging capability within a medical photoacoustic imaging camera system, in *Optical Tomography and Spectroscopy* (Optical Society of America, 2018), pp. OW4D–2
14. E. Rascevska, K.J. Joseph Francis, S. Manohar, Annular illumination photoacoustic probe for needle guidance in medical interventions, in *Opto-Acoustic Methods and Applications in Biophotonics IV*, vol. 11077 (International Society for Optics and Photonics, 2019), p. 110770L
15. J.L. Su, B. Wang, K.E. Wilson, C.L. Bayer, Y.S. Chen, S. Kim, K.A. Homan, S.Y. Emelianov, Advances in clinical and biomedical applications of photoacoustic imaging. Expert Opin. Med. Diagn. **4**(6), 497–510 (2010)
16. A. Fatima, K. Kratkiewicz, R. Manwar, M. Zafar, R. Zhang, B. Huang, N. Dadashzadesh, J. Xia, M. Avanaki, Review of cost reduction methods in photoacoustic computed tomography. Photoacoustics p. 100137 (2019)
17. M. Erfanzadeh, Q. Zhu, Photoacoustic imaging with low-cost sources: a review. Photoacoustics (2019)
18. Y. Zhu, G. Xu, J. Yuan, J. Jo, G. Gandikota, H. Demirci, T. Agano, N. Sato, Y. Shigeta, X. Wang, Light emitting diodes based photoacoustic imaging and potential clinical applications. Sci. Rep. **8**(1), 9885 (2018)

19. X. Wang, J.B. Fowlkes, J.M. Cannata, C. Hu, P.L. Carson, Photoacoustic imaging with a commercial ultrasound system and a custom probe. Ultrasound Med. Biol. **37**(3), 484–492 (2011)
20. L.V. Wang, Multiscale photoacoustic microscopy and computed tomography. Nat. Photonics **3**(9), 503 (2009)
21. C. Lutzweiler, D. Razansky, Optoacoustic imaging and tomography: reconstruction approaches and outstanding challenges in image performance and quantification. Sensors **13**(6), 7345–7384 (2013)
22. A.A. Oraevsky, V.A. Andreev, A.A. Karabutov, R.O. Esenaliev, Two-dimensional optoacoustic tomography: transducer array and image reconstruction algorithm, in *Laser-Tissue Interaction X: Photochemical, Photothermal, and Photomechanical*, vol. 3601, pp. 256–267 (International Society for Optics and Photonics, 1999)
23. G. Li, L. Li, L. Zhu, J. Xia, L.V. Wang, Multiview hilbert transformation for full-view photoacoustic computed tomography using a linear array. J. Biomed. Opt. **20**(6), 066010 (2015)
24. B.T. Cox, S.R. Arridge, P.C. Beard, Photoacoustic tomography with a limited-aperture planar sensor and a reverberant cavity. Inverse Prob. **23**(6), S95 (2007)
25. G. Li, J. Xia, K. Wang, K. Maslov, M.A. Anastasio, L.V. Wang, Tripling the detection view of high-frequency linear-array-based photoacoustic computed tomography by using two planar acoustic reflectors. Quant. Imaging Med. Surgery **5**(1), 57 (2015)
26. R.A. Kruger, W.L. Kiser Jr., D.R. Reinecke, G.A. Kruger, Thermoacoustic computed tomography using a conventional linear transducer array. Med. Phys. **30**(5), 856–860 (2003)
27. M. Oeri, W. Bost, S. Tretbar, M. Fournelle, Calibrated linear array-driven photoacoustic/ultrasound tomography. Ultrasound Med. Biol. **42**(11), 2697–2707 (2016)
28. K.J. Francis, B. Chinni, S.S. Channappayya, R. Pachamuthu, V.S. Dogra, N. Rao, Multiview spatial compounding using lens-based photoacoustic imaging system. Photoacoustics **13**, 85–94 (2019)
29. S. Agrawal, C. Fadden, A. Dangi, S.R. Kothapalli, Light-emitting-diode-based multispectral photoacoustic computed tomography system. Sensors **19**(22), 48–61 (2019)
30. J. Gateau, M.Á.A. Caballero, A. Dima, V. Ntziachristos, Three-dimensional optoacoustic tomography using a conventional ultrasound linear detector array: whole-body tomographic system for small animals. Med. Phys. **40**(1), 013302 (2013)
31. M. Omar, J. Rebling, K. Wicker, T. Schmitt-Manderbach, M. Schwarz, J. Gateau, H. López-Schier, T. Mappes, V. Ntziachristos, Optical imaging of post-embryonic zebrafish using multi orientation raster scan optoacoustic mesoscopy. Light Sci. Appl. **6**(1), e16186 (2017)
32. Y. Xu, L.V. Wang, G. Ambartsoumian, P. Kuchment, Reconstructions in limited-view thermoacoustic tomography. Med. Phys. **31**(4), 724–733 (2004)
33. K.J. Francis, Y. Boink, M. Dantuma, M.K.A. Singh, S. Manohar, W. Steenbergen, Tomographic imaging with an led-based photoacoustic and ultrasound system. Biomed. Opt. Express **11**(4) (2020) https://doi.org/10.1364/BOE.384548
34. B.E. Treeby, B.T. Cox, k-wave: Matlab toolbox for the simulation and reconstruction of photoacoustic wave fields. J. Biomed. Opt. **15**(2), 021314 (2010)
35. M. Jaeger, S. Schüpbach, A. Gertsch, M. Kitz, M. Frenz, Fourier reconstruction in optoacoustic imaging using truncated regularized inverse k-space interpolation. Inverse Prob. **23**(6), S51 (2007)
36. Z. Wang, A.C. Bovik, H.R. Sheikh, E.P. Simoncelli et al., Image quality assessment: from error visibility to structural similarity. IEEE Trans. Image Process. **13**(4), 600–612 (2004)
37. H.J. Kang, M.A.L. Bell, X. Guo, E.M. Boctor, Spatial angular compounding of photoacoustic images. IEEE Trans. Med. Imaging **35**(8), 1845–1855 (2016)
38. K.J. Francis, B. Chinni, S.S. Channappayya, R. Pachamuthu, V.S. Dogra, N. Rao, Two-sided residual refocusing for an acoustic lens-based photoacoustic imaging system. Phys. Med. Biol. **63**(13), 13NT03 (2018)
39. K.J. Francis, B. Chinni, S.S. Channappayya, R. Pachamuthu, V.S. Dogra, N. Rao, Characterization of lens based photoacoustic imaging system. Photoacoustics **8**, 37–47 (2017)

40. S. Ma, S. Yang, H. Guo, Limited-view photoacoustic imaging based on linear-array detection and filtered mean-backprojection-iterative reconstruction. J. Appl. Phys. **106**(12), 123104 (2009)
41. R.A. Kruger, P. Liu, Y.R. Fang, C.R. Appledorn, Photoacoustic ultrasound (paus)–reconstruction tomography. Med. Phys. **22**(10), 1605–1609 (1995)
42. D. Yang, D. Xing, S. Yang, L. Xiang, Fast full-view photoacoustic imaging by combined scanning with a linear transducer array. Opt. Express **15**(23), 15566–15575 (2007)
43. J. Gamelin, A. Maurudis, A. Aguirre, F. Huang, P. Guo, L.V. Wang, Q. Zhu, A real-time photoacoustic tomography system for small animals. Opt. Express **17**(13), 10489–10498 (2009)
44. L. Yu, F. Nina-Paravecino, D.R. Kaeli, Q. Fang, Scalable and massively parallel monte carlo photon transport simulations for heterogeneous computing platforms. J. Biomed. Opt. **23**(1), 010504 (2018)
45. S.L. Jacques, Optical properties of biological tissues: a review. Phys. Med. Biol. **58**(11), R37 (2013)
46. J. Staal, M.D. Abràmoff, M. Niemeijer, M.A. Viergever, B. Van Ginneken, Ridge-based vessel segmentation in color images of the retina. IEEE Trans. Med. Imaging **23**(4), 501–509 (2004)
47. Y.E. Boink, M.J. Lagerwerf, W. Steenbergen, S.A. Van Gils, S. Manohar, C. Brune, A framework for directional and higher-order reconstruction in photoacoustic tomography. Phys. Med. Biol. **63**(4), 045018 (2018)
48. G. Xu, J.R. Rajian, G. Girish, M.J. Kaplan, J.B. Fowlkes, P.L. Carson, X. Wang, Photoacoustic and ultrasound dual-modality imaging of human peripheral joints. J. Biomed. Opt. **18**(1), 010502 (2012)
49. P.J. van den Berg, K. Daoudi, H.J.B. Moens, W. Steenbergen, Feasibility of photoacoustic/ultrasound imaging of synovitis in finger joints using a point-of-care system. Photoacoustics **8**, 8–14 (2017)
50. J.R. Rajian, X. Shao, D.L. Chamberland, X. Wang, Characterization and treatment monitoring of inflammatory arthritis by photoacoustic imaging: a study on adjuvant-induced arthritis rat model. Biomed. Opt. Express **4**(6), 900–908 (2013)
51. J. Jo, G. Xu, Y. Zhu, M. Burton, J. Sarazin, E. Schiopu, G. Gandikota, X. Wang, Detecting joint inflammation by an led-based photoacoustic imaging system: a feasibility study. J. Biomed. Opt. **23**(11), 110501 (2018)
52. P. van Es, S.K. Biswas, H.J.B. Moens, W. Steenbergen, S. Manohar, Initial results of finger imaging using photoacoustic computed tomography. J. Biomed. Opt. **19**(6), 060501 (2014)
53. M. Nishiyama, T. Namita, K. Kondo, M. Yamakawa, T. Shiina, Ring-array photoacoustic tomography for imaging human finger vasculature. J. Biomed. Opt. **24**(9), 096005 (2019)